JGR Oceans

RESEARCH ARTICLE
10.1029/2020JC016592

Key Points:

- Observational transport time series of the Atlantic Subtropical Cells reveals dominant seasonal variability for horizontal branches
- On time scales longer than ~5 years, interior thermocline layer transport convergence modulates equatorial sea surface temperature anomalies
- Western boundary current and interior transport anomalies are partly compensating each other at thermocline level on all time scales

Supporting Information:

- Supporting Information S1

Correspondence to:
F. P. Tuchen,
ftuchen@geomar.de

Citation:
Tuchen, F. P., Lübbecke, J. F., Brandt, P., & Fu, Y. (2020). Observed transport variability of the Atlantic Subtropical Cells and their connection to tropical sea surface temperature variability. *Journal of Geophysical Research: Oceans*, *125*, e2020JC016592. https://doi.org/10.1029/2020JC016592

Received 10 JUL 2020
Accepted 18 NOV 2020

Observed Transport Variability of the Atlantic Subtropical Cells and Their Connection to Tropical Sea Surface Temperature Variability

Franz Philip Tuchen[1], Joke F. Lübbecke[1,2], Peter Brandt[1,2], and Yao Fu[3]

[1]GEOMAR Helmholtz Centre for Ocean Research Kiel, Kiel, Germany, [2]Faculty of Mathematics and Natural Sciences, Kiel University, Kiel, Germany, [3]State Key Laboratory of Tropical Oceanography, South China Sea Institute of Oceanology, Chinese Academy of Sciences, Guangzhou, China

Abstract The shallow meridional overturning cells of the Atlantic Ocean, the subtropical cells (STCs), consist of poleward Ekman transport at the surface, subduction in the subtropics, equatorward flow at thermocline level and upwelling along the equator and at the eastern boundary. In this study, we provide the first observational estimate of transport variability associated with the horizontal branches of the Atlantic STCs in both hemispheres based on Argo float data and supplemented by reanalysis products. Thermocline layer transport convergence and surface layer transport divergence between 10°N and 10°S are dominated by seasonal variability. Meridional thermocline layer transport anomalies at the western boundary and in the interior basin are anti-correlated and partially compensate each other at all resolved time scales. It is suggested that the seesaw-like relation is forced by the large-scale off-equatorial wind stress changes through low-baroclinic-mode Rossby wave adjustment. We further show that anomalies of the thermocline layer interior transport convergence modulate sea surface temperature (SST) variability in the upwelling regions along the equator and at the eastern boundary at time scales longer than 5 years. Phases of weaker (stronger) interior transport are associated with phases of higher (lower) equatorial SST. At these time scales, STC transport variability is forced by off-equatorial wind stress changes, especially by those in the southern hemisphere. At shorter time scales, equatorial SST anomalies are, instead, mainly forced by local changes of zonal wind stress.

Plain Language Summary In both hemispheres of the Atlantic Ocean, shallow meridional overturning circulations provide a connection between the subtropics and equatorial upwelling regions. The so-called subtropical cells (STCs) consist of poleward transport at the surface driven by the easterly trade winds, subduction in the subtropics, equatorward flow at subsurface level and upwelling along the equator and at the eastern boundary. In this study, we provide the first observational time series of transport variability associated with the horizontal branches of the STCs estimated at 10°N and 10°S. It shows that both branches are dominated by variability on seasonal time scales. On longer time scales, transport anomalies at the western boundary reveal a reversed relation to transport anomalies in the interior leading to partial compensation. It is suggested that transport anomalies are affected by adjustment to wind-forced oceanic planetary waves. We further show that the interior part of the subsurface transport anomalies is connected to equatorial sea surface temperature (SST) anomalies at time scales longer than 5 years. There, stronger (weaker) equatorward transport is associated with negative (positive) equatorial SST anomalies. At shorter time scales, equatorial SST anomalies are, instead, mainly forced by changes of local wind stress.

1. Introduction

The shallow tropical Atlantic Ocean is characterized by a superposition of the wind-driven and thermohaline circulation (e.g., Schott et al., 2004). Most prominently, the warm water return flow of the Atlantic meridional overturning circulation (AMOC) crosses the equator on its northward pathway along the Brazilian coast, as part of the North Brazil Undercurrent (NBUC)/North Brazil Current (Stramma et al., 1995). Superimposed on the uppermost part of the AMOC return flow are shallow meridional overturning circulations, referred to as the subtropical cells (STCs), that connect the subduction zones of the subtropical gyres with the equatorial and eastern tropical upwelling regions (Liu et al., 1994; Luyten et al., 1983; McCreary

& Lu, 1994). The STCs are confined to approximately the upper 300 m and are forced by equatorial Ekman divergence due to the easterly trade winds. In a zonal average of each hemisphere, they consist of poleward Ekman transport in the surface layer, subduction in the subtropics, equatorward geostrophic transport at thermocline level and are eventually closed by upwelling along the equator and at the eastern boundary (e.g., Fratantoni et al., 2000; Malanotte-Rizzoli et al., 2000; Schott et al., 2004). As a consequence of the superposition of STCs and AMOC at the western boundary, an interhemispheric asymmetry in terms of mean equatorward STC transport at thermocline level exists in which the southern hemisphere STC carries about 2–3 times more water toward the equator than its counterpart in the northern hemisphere (Fratantoni et al., 2000; Tuchen et al., 2019; Zhang et al., 2003). Besides this interhemispheric asymmetry, the mean state of the Atlantic STCs further exhibits a zonal asymmetry between equatorward transport at the western boundary and in the interior basin in both hemispheres (Tuchen et al., 2019; Zhang et al., 2003). Generally, the western boundary pathways contribute more to the overall thermocline layer transport convergence due to both a limitation of interior transport in the northern hemisphere caused by a potential vorticity ridge (Malanotte-Rizzoli et al., 2000) and a strong western boundary current in the southern hemisphere supported by the AMOC return flow (Schott et al., 2002). However, a general lack of Argo observations at the shelf and continental slope and diverging results from model simulations of western boundary current transport introduce a considerable uncertainty when compared to one of the few observational long-term records along 11°S (Hummels et al., 2015; Tuchen et al., 2019). While there have been several studies describing the mean state of the Atlantic STCs both from a model (e.g., Hazeleger & Drijfhout, 2006; Hazeleger et al., 2003) and from an observational perspective (Tuchen et al., 2019; Zhang et al., 2003), little is known about the temporal variability of the Atlantic STCs.

The majority of studies on STC variability has focused on the Pacific STCs. From these studies, two findings stand out: First, numerical studies show that on interannual to decadal time scales transport anomalies at the western boundary and in the interior basin are anti-correlated showing a seesaw-like relation (Capotondi et al., 2005; Lee & Fukumori, 2003; Schott et al., 2007). On these time scales western boundary and interior transport anomalies partly compensate each other. Lee and Fukumori (2003) attribute the partial compensation to two different mechanisms: changes at the western boundary are suggested to be forced by adjustment to variations in Ekman pumping while interior transport changes are associated with near-equatorial wind stress changes. In contrast, Capotondi et al. (2005) argue that both western boundary and interior transport variations are associated with baroclinic adjustment to Rossby waves due to large scale changes of the wind stress curl. Knowledge about this anti-correlation is based on numerical studies for the Pacific Ocean and has so far not been shown for the Atlantic Ocean. Second, in observational (McPhaden & Zhang, 2002, 2004) and numerical studies (Farneti et al., 2014; Lübbecke et al., 2008; Zhang & McPhaden, 2006), it has been shown that decadal transport variations of the Pacific STCs can be linked to decadal tropical sea surface temperature (SST) variability. Phases of anomalously large STC transport coincide with phases of anomalously low tropical Pacific SST and vice versa (e.g., McPhaden & Zhang, 2002, 2004).

Two possible mechanisms on how the STCs could drive SST variability have been proposed. First, Gu and Philander (1997) described how temperature anomalies are subducted in the subtropics and transported equatorward by a constant geostrophic transport as part of the lower branch of the STCs ($\overline{v}T'$ mechanism; with v being the meridional transport and T the temperature with the overbar marking the mean and the prime marking anomalies relative to the mean). This scenario implies that subducted temperature anomalies are observed in the upwelling regions with a considerable time lag. In fact, travel times of subducted particles could range from years to even decades when considering the possibility of multiple recirculations before eventually reaching the upwelling areas. In the second mechanism, subducted water with constant temperature is brought toward the tropics by an anomalously strong or weak equatorward thermocline layer transport ($v'\overline{T}$ mechanism; Kleeman et al., 1999). It is proposed that the rate at which subtropical water is transported toward the tropics rather than its temperature anomaly drives tropical SST anomalies by dynamical changes in the equatorial and eastern boundary upwelling rate. The $v'\overline{T}$ mechanism could explain the fast response of SST anomalies to transport changes described in previous studies. For the Pacific Ocean, the model study of Hazeleger et al. (2001) could show that the response of tropical temperature anomalies to extra-tropical forcing is small and rather local wind stress anomalies are suggested to drive variability both in the subtropics and tropics. Based on this and other studies, the $v'\overline{T}$ mechanism by

Kleeman et al. (1999) is deemed more likely (e.g., McPhaden & Zhang, 2002; Schott et al., 2004). However, in the model by Kleeman et al. (1999), tropical SST anomalies are mainly driven by subtropical wind stress changes (poleward of ~23°) whereas Nonaka et al. (2002) show that equatorial wind stress variability plays an equally important role in modulating equatorial SST anomalies on interannual to decadal time scales. Recently, Graffino et al. (2019) analyzed the role of differing magnitudes and locations of wind stress forcing in driving Pacific STC and SST variability. They conclude that equatorial wind stress anomalies are not responsible for STC changes but force local SST anomalies through thermocline adjustment to local wind stress anomalies, whereas subtropical wind stress anomalies have the strongest impact on changes in STC transport.

To date, studies on STC transport variability in the Atlantic Ocean have been limited to using either a forced ocean model (Hüttl & Böning, 2006) or an ocean assimilation model (Rabe et al., 2008). These studies focused mainly on the impact on the equatorial current system. Rabe et al. (2008) suggest that the STCs and the Equatorial Undercurrent (EUC) are connected on pentadal (5 years) and longer time scales. In a so-called loop response, changes in the wind-driven surface branches of the STCs, first lead to a response in the EUC followed by changes in the thermocline layer transport convergence.

On global warming time scales, Luo et al. (2009) found for the Pacific that, due to an expected westward shift of the potential vorticity barriers, the thermocline layer transport near the western boundary increases while the interior transport decreases. These opposed transport trends appear to compensate each other resulting in no significant change in the total equatorward STC transport. On comparable time scales, Oschlies et al. (2018) suggested that the ventilated tropical thermocline becomes shallower and thinner leading to reduced oxygen undersaturation in upwelling regions and thus to a reduction in oxygen uptake emphasizing the possible role of the STCs in ocean deoxygenation.

Since the start of the Argo program in the early 2000s, the number of observational hydrographic data in all oceans increased dramatically and has already been used to derive a realistic mean state of the Atlantic STCs (Tuchen et al., 2019). The first aim of this study is to provide transport time series of the horizontal STC branches from observations such as Argo float data, moored velocity data at the western boundary and satellite wind data accompanied by reanalysis products to extend the analysis further into the past. The dominant temporal scales of transport variability of the horizontal STC branches and their components are identified followed by a quantification of both the relation between thermocline layer transport anomalies at the western boundary and in the interior and the relation between STC transport variability and SST variability in the tropical Atlantic Ocean. SST fluctuations are known to have considerable effects on various climate parameters. On interannual and decadal time scales tropical Atlantic SST anomalies are connected to climate hazards such as extreme rainfall or droughts both over Brazil and Africa (e.g., Carton et al., 1996) mostly associated with the meridional or zonal mode. Therefore, skillful prediction of tropical SST variations has been the subject of numerous studies in order to better forecast future extreme events (e.g., Chang et al., 1998).

The present study is structured as follows. Section 2 describes the data products which were used to derive the transport time series of the horizontal branches of the STCs and the SST time series. Section 3 provides an overview of the methods. In Section 4, we present the results which are divided into a description of the observed transport variability, the relation between western boundary and interior transport anomalies and the connection of STC variability to tropical SST variability. The presented results are then summarized and complemented with a conclusion in Section 5.

2. Data

In this section, we provide an overview of the data that were used in this study. Transports at thermocline level are mainly derived from hydrographic data from the Roemmich-Gilson Argo climatology (from here on referred to asRG-clim; Roemmich & Gilson, 2009) and from the ECMWF Ocean Reanalysis System version 4 (ORAS4; Balmaseda et al., 2013). RG-clim and ORAS4 provide monthly temperature and salinity data on a $1° \times 1°$ grid for a time period from 2004 to 2019 (RG-clim) and 1980 to 2017 (ORAS4), respectively. Additionally, ORAS4 provides horizontal ocean velocities. The surface flux forcing of ORAS4 consists of daily surface fluxes of heat, momentum and freshwater from ERA-40 (prior to 1989), ERA-interim (1989–2009)

and from the operational ECMWF atmospheric reanalysis (from 2010 onwards; Balmaseda et al., 2013). Under the assumption that below the wind-driven surface layer the flow is generally in geostrophic balance we use total velocities from ORAS4 for comparison with the geostrophic velocities derived from RG-clim. In order to quantify transport uncertainties at the western boundary due to sparse coverage by Argo floats, thermocline layer transport calculations in the southern hemisphere are complemented by moored velocity data at 11°S from 2013 to 2018 (update of Hummels et al., 2015). At 11°S, four moorings – arranged on a cross-shore array — have been operating from 2013 to present. The moorings are located at isobaths well below the lower boundary of the STC at ∼: 900, 2,320, 3,520, and 4,110 m. By applying a gap filling method described in Schott et al. (2005) and Hummels et al. (2015) an alongshore velocity data set with a temporal resolution of 2.5 days and a spatial resolution of 5 km (horizontal) and 10 m (vertical) is derived.

Ekman transports are calculated from ocean surface wind speed data (typically 10 m above sea surface). Here, we use two long-term reanalysis products with a monthly resolution, ERA-interim (Dee et al., 2011) and ERA5 (Hersbach & Dee, 2016), and two consecutive satellite scatterometer missions with weekly resolution and an overlap of about 2.5 years, QuikSCAT (Ricciardulli et al., 2011) from July 1999 to November 2009 and Advanced Scatterometer (ASCAT; Ricciardulli & Wentz, 2016) from March 2007 to present. Both wind reanalysis products span the time period from 1980 to 2019. ERA-interim is being phased out and data stopped in August 2019 whereas ERA5 provides data to present. All wind products are provided at a 1/4° horizontal resolution.

To analyze the link between STC transport variability and tropical SST variability on interannual to decadal time scales, SST time series from the Optimum Interpolation SST Analysis Version 2 (OI-SST; Reynolds et al., 2007) are used. Daily maps with a horizontal resolution of 1/4° are provided from January 1982 to present.

3. Methods

3.1. Thermocline Transport

Equatorward transport within the thermocline layer is primarily associated with geostrophic flow. However, geostrophic flow is also present above the thermocline layer where it reduces the wind-driven poleward transport in the tropics (Schott et al., 2004). In order to derive geostrophic transports from hydrographic properties we mainly follow the approach of Tuchen et al. (2019) and only give a brief overview of their methods and definitions of the horizontal STC branches here. In a first step, hydrography from RG-clim and ORAS4 are used to obtain maps of dynamic height anomalies for the tropical Atlantic Ocean. From the zonal pressure gradient, which is a consequence of zonal differences in dynamic height anomalies, meridional geostrophic velocities relative to a level of no motion at 1,000 dbar are calculated. Zonal geostrophic velocities are derived analogously from the meridional gradient of dynamic height anomalies. Here, we reference relative geostrophic velocities from RG-clim by prescribing the time-mean (2004–2019) horizontal velocity from Argo float displacements within a parking pressure level range between 850 and 1,150 dbar as the reference velocity at 1,000 dbar taken from the updated YoMaHa`07 data set (Lebedev et al., 2007). Therefore, horizontal displacement values are binned and averaged in 1 × 1° boxes before being spatially smoothed with an objective mapping routine (influence radius of 2° and cut-off radius of 4°). The mean meridional velocity at depth is close to zero along 10°N and 10°S and only shows significant southward velocities at the western boundary at 10°N (Figure S1). To account for those, we decided to reference relative geostrophic velocities with the mean meridional velocity instead of assuming a level of no motion at depth. However, the difference between both approaches is marginal. It has to be noted that the temporal and spatial coverage by Argo float displacement data is not sufficient to facilitate reliable monthly values. Close to the western boundary, coverage by Argo floats is naturally sparse and RG-clim fails to resolve the westernmost part of the tropical Atlantic introducing a transport uncertainty which has already been described in Tuchen et al. (2019). Here, we address the transport uncertainty at the western boundary by comparison to moored velocity data along 11°S and to velocity data provided by ORAS4. In the mean state, ORAS4 and mean ship section data along 11°S both reveal an underestimation of transport of about 2 Sv at the western boundary in the southern hemisphere by Argo float data (Tuchen et al., 2019). At 10°N, there is no comparable observational data set for the northern hemisphere western boundary transport. However, meridional geostrophic velocity from Argo float data shows a mean northward transport west of 55°W which appears to

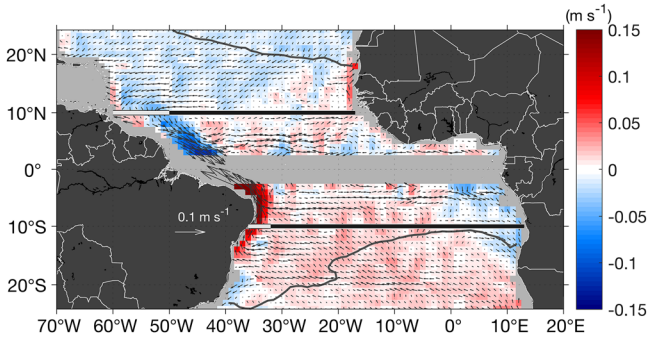

Figure 1. Mean absolute geostrophic velocities in the tropical Atlantic Ocean between 2004 and 2019 within the thermocline layer (25.5 kg m^{-3} isopycnal) derived from the Roemmich & Gilson Argo climatology (Roemmich & Gilson, 2009). Arrows show the horizontal absolute geostrophic velocity; the color shading indicates the magnitude of the meridional component of the absolute geostrophic velocity with red (blue) showing northward (southward) flow. The seasonal outcropping of the 25.5 kg m^{-3} isopycnal is superimposed (dark gray isoline) in both hemispheres. Zonal sections at 10°N and 10°S are divided into a western boundary (white line) and an interior part (black line) at 50°W and 32°W, respectively.

be cut off due to insufficient data coverage. It is therefore suggested that meridional transport from Argo float data rather overestimates the mean zonally accumulated equatorward transport at 10°N by missing parts of the northward transport at the western boundary.

Geostrophic transport derived from the hydrographic properties of ORAS4 is also missing the westernmost part of the western boundaries due to the calculation of meridional geostrophic velocities between zonal grid points of temperature and salinity leading to an overall reduction of 0.5° at each site of the basin. While RG-clim is referenced to the mean meridional velocity from Argo float displacements, we use 370 dbar temporally varying velocities provided by ORAS4 to reference geostrophic velocities derived from the hydrographic properties in ORAS4. This pressure level is chosen in order to cover as many grid points as possible at the western boundary that are deeper than the lower boundary of the STCs.

Finally, thermocline layer transports at 10°N and 10°S are derived by integrating meridional geostrophic velocities between a lower (26.0 kg m^{-3} isopycnal) and an upper boundary (seasonally varying depth between 30 and 70 m) following Tuchen et al. (2019). At 26.0 kg m^{-3} the sign of the zonally averaged meridional geostrophic transport reverses. This is true for both the mean state and for the time series (not shown). Seasonal outcropping of isopycnals of the thermocline layer is only observed in the eastern parts of the subtropics and is treated as an absence of thermocline layer transport in our calculation. However, the surface layer transport, which is chosen according to the depth at which the absolute meridional velocity from ORAS4 changes its sign from poleward to equatorward, is unaffected by outcropping of isopycnals as it is bounded by depth. In the case of the 11°S moored velocity data, the lower boundary of the thermocline layer is derived from the mean density field of five cross-shore ship sections along the mooring array (26.0 kg m^{-3} isopycnal as well). The upper boundary is set to 60 m which marks the zonally averaged annual mean depth of meridional velocity reversal from ORA-S4 at this latitude (Tuchen et al., 2019).

Within the thermocline layer, the pattern of the mean horizontal geostrophic velocity from Argo float data reveals the pathways of the equatorward branches of the STCs (Figure 1) which are in good agreement with total velocities from ORAS4 (Figure S2). At around 15°S, the bifurcation of the South Equatorial Current into the northward flowing NBUC and the southward flowing Brazil Current marks the division between subducted water moving equatorward as part of the southern STC or AMOC and water being recirculated within the subtropical gyre of the southern hemisphere. The southern section at 10°S is therefore chosen to be equatorward of the bifurcation area (see Figure 1). The southern STC exhibits a substantial longitudinal range in the interior basin with equatorward velocities in the 16-year Argo climatological mean. In contrast, the interior pathway is largely limited in the northern hemisphere by the mean position of the Intertropical Convergence Zone and the resulting potential vorticity barrier (Malanotte-Rizzoli et al., 2000). In order to examine the variability of STC transport in more detail, the zonal sections at 10°N and 10°S, at which transport time series are derived, are divided into a western boundary and an interior part at 50°W (32°W) at 10°N (10°S) as indicated in Figure 1.

3.2. Ekman and Surface Layer Transport

Poleward transport in the surface layer of the tropical Atlantic is mainly driven by the north- and south-easterly trade winds forcing poleward Ekman transport in both hemispheres and leading to Ekman divergence at the equator. Here, we use four different wind products which provide zonal and meridional wind speed at 10 m height above the sea surface. From wind speed ($\mathbf{u}$), we obtain wind stress (τ) via the Bulk formula calculation:

$$\boldsymbol{\tau} = \rho_a * c_d * |\boldsymbol{u}| * \boldsymbol{u}$$

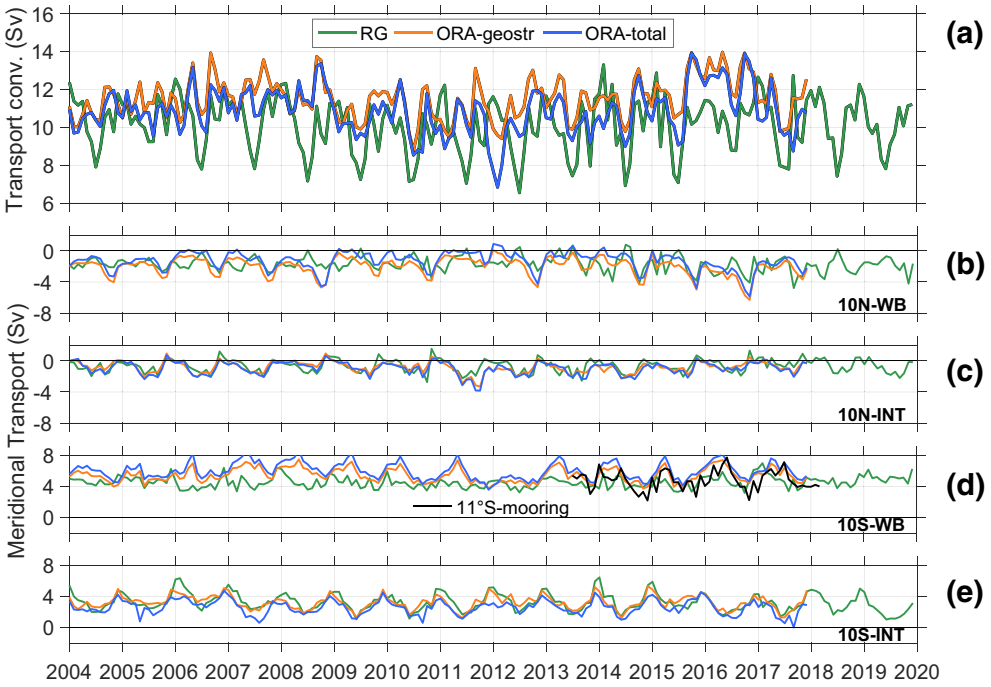

Figure 2. Monthly time series of (a) thermocline layer transport convergence between 10°N and 10°S from RG-clim (green), from the geostrophic component of ORAS4 (orange) and from total ORAS4 (blue) and thermocline layer transport (b) along the western boundary at 10°N, (c) within the interior at 10°N, (d) along the western boundary at 10°S and (e) within the interior at 10°S. Note that the 11°S mooring transport time series in (d) is calculated between 35.85°W and 33.85°W. Positive (negative) values indicate northward (southward) transport (b–e).

using a reference density $\rho_a = 1.22$ kg m^{-3} and a drag coefficient $c_d = 0.0013$. Meridional Ekman transport is a function of zonal wind stress and the latitude-dependent Coriolis parameter. In the cases of ASCAT and QuikSCAT, wind stress data are provided on a weekly basis and for the purpose of this study monthly means are derived for all months that provide at least four data points.

In the surface layer of the tropical interior oceans, poleward Ekman transport opposes generally equatorward geostrophic transport due to zonal pressure gradients. Therefore, when combining both components, we refer to the net surface layer transport divergence since the Ekman divergence dominates the surface layer but is reduced by the geostrophic convergence. Different approaches are compared: surface layer transports are derived directly from velocity data (ORAS4 and 11°S mooring) or calculated as the sum of Ekman transport and geostrophic transport. The lower boundary of the surface layer is the same seasonally varying depth used as the upper boundary for the thermocline layer as described in Section 3.1.

4. Results

4.1. Transport Variability of the Horizontal STC Branches

Monthly thermocline layer transports are derived and summed up along the zonal sections at 10°N and 10°S, from the eastern to the western boundary. The difference between both hemispheres yields the monthly thermocline layer transport convergence time series (Figure 2a). Transport convergences vary between ~7 and 14 Sv. In general, we find good agreement between ORAS4 and ORAS4-geostr as expected. However, there are larger differences between the geostrophic transport of RG-clim and both ORAS4-based products which mainly originate from differences at the western boundary (Figures 2b and 2d). As already indicated in Figure 2a the dominant signal in all time series is the seasonal cycle with a minimum in boreal summer and a maximum in boreal winter which is most pronounced in RG-clim. A spectral analysis (not shown) confirms the dominance of the annual signal but also reveals elevated variability at the semiannual cycle and the 120-day period. At periods longer than 1 year, no spectral peaks that are significant against an AR-1

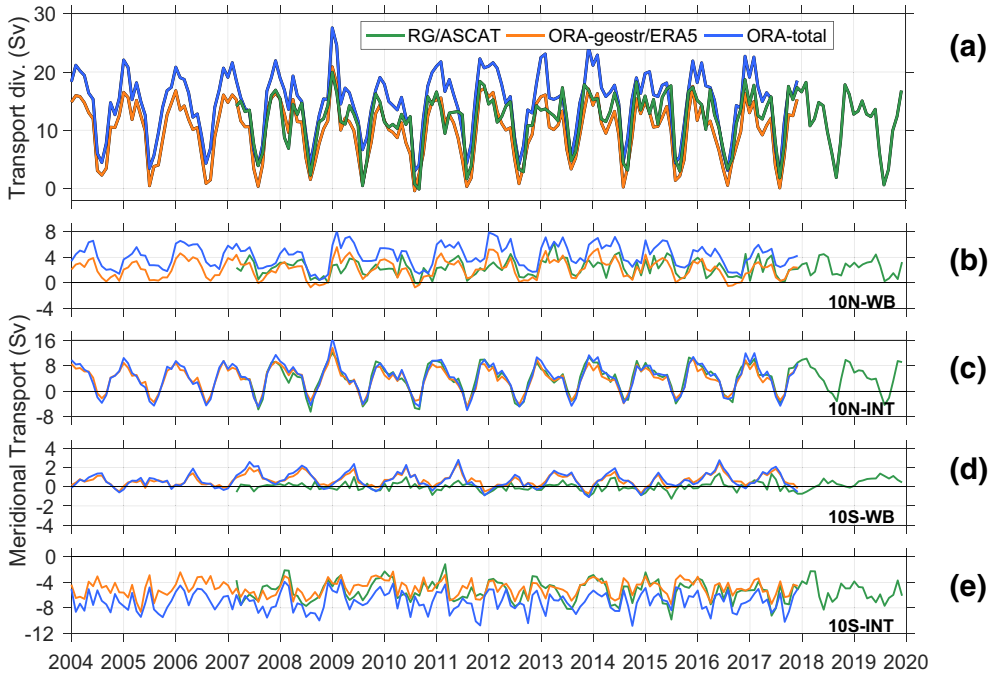

Figure 3. Monthly time series of (a) net surface layer transport divergence (geostrophy + Ekman) between 10°N and 10°S from RG-clim/ASCAT (green), from ORAS4/ERA5 (orange), and total ORAS4 (blue), meridional surface layer net transport (b) along the western boundary at 10°N, (c) within the interior at 10°N, (d) along the western boundary at 10°S, and (e) within the interior at 10°S. Positive (negative) values indicate northward (southward) transport (b–e).

red noise spectrum could be observed. Nevertheless, interannual and longer-period fluctuations are evident throughout the time series. For instance, we observe a transport convergence weakening from 2005 until about 2010 followed by a strengthening until about 2016. Interannual transport fluctuations will be further discussed in the next sections.

By separating the thermocline layer transport convergence into its components at 10°N and 10°S, both further divided into a western boundary and an interior contribution (see also Figure 1), good agreement between the three products in the interior parts is observed (Figures 2c and 2e), whereas especially the southern hemisphere western boundary transport reveals obvious differences between RG-clim and the ORAS4 products. This is mainly due to a better coverage of the western boundary by ORAS4 leading to both enhanced northward western boundary transport at 10°N (Figure 2b) and reduced equatorward transport at 10°S (Figure 2d).

When comparing western boundary transport in the southern hemisphere from ORAS4 to mooring data at around 11°S, we find a comparable seasonal evolution and magnitude (Figure 2d). Note that the 11°S-mooring transport is limited to longitudes west of about 33.85°W. However, when considering thermocline layer transports from ORAS4-geostr only between 36°W and 34°W, both time series still agree well (not shown). In contrast, thermocline layer transport at the western boundary derived from RG-clim appears to underestimate this particular branch of the STCs. Thermocline layer meridional transport is on average southward in the northern hemisphere with occasional transport reversals both at the western boundary and in the interior basin (Figures 2b and 2c). In comparison, transport in the southern hemisphere is generally stronger and persistently northward throughout the presented time period (Figures 2d and 2e).

Above the thermocline layer, equatorward geostrophic transport is largely exceeded by the wind-driven poleward Ekman transport. In total, a net surface layer transport divergence exists between 10°N and 10°S (Figure 3a). Here, we subtract the geostrophic transport convergence of RG-clim (ORAS4-geostr) from the Ekman divergence of ASCAT (ERA5) for the period in which the particular time series overlap. In addition, surface layer transports are directly calculated from total velocities provided by ORAS4. All products agree well on the seasonality which is mainly in phase with the seasonal evolution of the thermocline layer

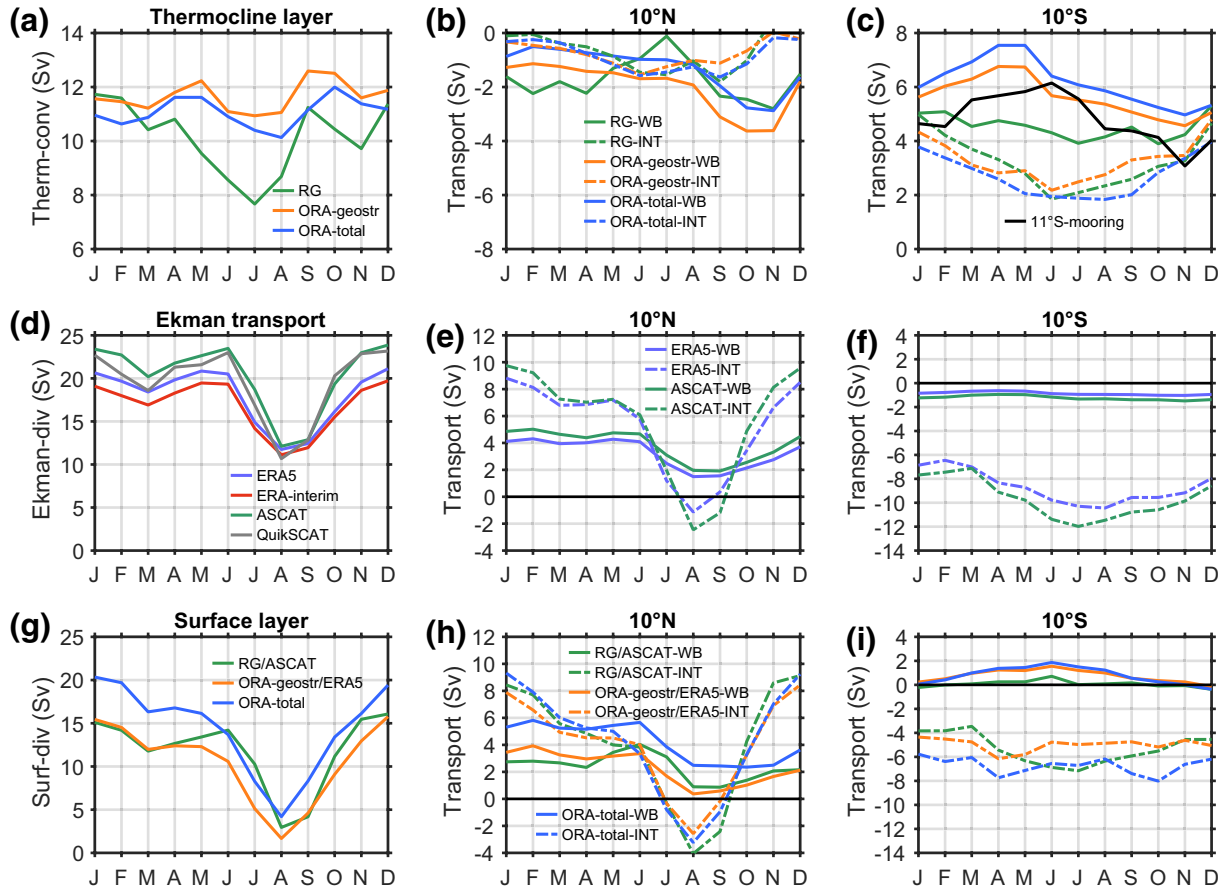

Figure 4. Monthly climatology of (a) thermocline layer transport convergence, (d) Ekman divergence, and (g) net surface layer transport divergence. Panels (a, d, and g) are further separated into their individual transport components at 10°N (b, e, and h) and 10°S (c, f, and i). In each hemisphere, the transports are divided into a western boundary (WB, solid lines) and an interior (INT, dashed lines) transport contribution.

transport convergence: a maximum in boreal winter and a minimum in boreal summer. However, analogously to the thermocline layer, the largest differences in magnitude are observed at the western boundary in both hemispheres (Figures 3b and 3d) while interior transports show good agreement (Figures 3c and 3e). At 10°S, geostrophic transport in the surface layer is northward at the western boundary (Figure 2d) compensating the poleward Ekman transport (Figure 3d), while western boundary surface layer transport at 10°N is mainly northward supporting the wind-driven transport (Figure 3b). Note that due to the small zonal extent of the western boundary component as part of the zonal sections along 10°N and, especially, 10°S, the Ekman transport component is rather small compared to Ekman transport in the interior which is cumulated over a larger distance. Besides the dominant annual and semiannual cycle, again, no statistically significant spectral peaks are present at interannual to decadal time scales, although a similar oscillation as described before for the thermocline layer transport convergence can be observed: a minimum of transport divergence at around 2010 is followed by a strengthening until about 2013.

The relative importance of the representation of the western boundary in the data products becomes even more obvious in the climatological cycles of the thermocline layer and surface layer transport components (Figure 4). In the thermocline layer, the seasonal cycle is most pronounced in RG-clim with minimum convergence values around 8 Sv in boreal summer (Figure 4a). This is due to a distinct minimum of equatorward transport at 10°N at the western boundary in boreal summer which is not reproduced in the ORAS4 products (Figure 4b). Generally, in both hemispheres all three products agree well for the interior but show considerable differences at the western boundary (Figures 4b and 4c). The differences between the two transport estimates based on ORAS4 must essentially originate from the 0.5° data loss that the geostrophic transport derivation requires and emphasizes the importance of a high-resolved representation of the

western boundary. Overall, at thermocline level, the climatological cycles from RG-clim suggest that the seasonal cycle of the convergence is mainly driven by the seasonality at the western boundary in the north and the interior in the south which shows concurrent minimum equatorward transport in boreal summer.

The Ekman divergence climatologies are calculated for the four different wind products which all agree well on the seasonality (Figure 4d) and show some difference in magnitude away from the annual minimum which occurs in late boreal summer. The seasonal cycle of Ekman divergence exhibits peak-to-peak amplitudes of more than 10 Sv and is mainly driven by the northern hemisphere interior component where Ekman transports even reverse to equatorward transport to show a distinct minimum during late boreal summer (Figure 4e). However, besides a statistically significant annual cycle, we also observe a semiannual cycle likely due to a relative minimum of poleward Ekman transport in the interior at 10°N in boreal spring superimposed by a minimum in February/March in the interior at 10°S. In general, all four components of the Ekman divergence (Figures 4e and 4f) are in good agreement in terms of the temporal evolution of the seasonal cycle while their magnitudes reveal differences comparable to the western boundary thermocline layer.

In the following, because of the good agreement between all wind products, further analysis involving Ekman transports is carried out using data from one reanalysis product (ERA5) and one satellite product (ASCAT) only. ASCAT aligns better in time with RG-clim compared to QuikSCAT. It has been recently shown that — in terms of wind speed agreement with ASCAT observations - ERA5 winds provide a 20% improvement in comparison to ERA-interim (Belmonte Rivas & Stoffelen, 2019).

As previously described, the overall surface layer transport is a combination of Ekman transport and geostrophic transport. Here, we estimate both components individually and also compare them to surface layer transports directly derived from ORAS4 (Figure 4g). Since the Ekman transport dominates the surface layer, all products show poleward transport throughout the whole year leading to an overall surface layer divergence while also agreeing on the same seasonality as the Ekman divergence (Figure 4d). The geostrophic component reduces all four transport components in the surface layer to less poleward or even equatorward. In the southern hemisphere, the strong northward western boundary current exceeds the southward Ekman transport in the surface layer and shows an overall equatorward transport of up to 2 Sv in boreal summer (Figure 4i).

4.2. Western Boundary Versus Interior Transport Anomalies

As shown in the previous section, the thermocline layer transport convergence and the net surface layer transport divergence vary dominantly on seasonal time scales with a modulation on interannual and longer scales. In this section, we will show that even though interannual variability of the total thermocline layer transport convergence might be relatively weak, interannual transport anomalies at the western boundary and in the interior basin show a remarkable relation. First, we separate the thermocline layer transport convergence time series into the western boundary and the interior components in both hemispheres (at the longitudes indicated in Figure 1) before filtering out the dominating seasonal signal by applying a 2-year running mean.

In both hemispheres, the time series of interannual transport fluctuations at the western boundary (WB) and in the interior (INT) are out of phase for both RG-clim and ORAS4-geostr (Figure 5). Transport anomalies at the western boundaries and anomalies in the interior basin are highly anti-correlated on interannual time scales and as a result partly compensate each other. In the northern hemisphere, maximum cross-correlation coefficients are as high as −0.78 for RG-clim (Figure 5a) and −0.43 for ORAS4-geostr (Figure 5c), respectively.

Note that the anti-correlation in ORAS4-geostr is more pronounced in the later phase of the time series that overlaps with RG-clim. The observed WB-INT relation can essentially be described as a seesaw in which the two components are generally in opposite phases. For both products, meridional transport anomalies in the interior reach about ±0.3 Sv and are slightly smaller compared to western boundary transport anomalies (up to ±0.5 Sv and occasionally above at the western boundary in ORAS4-geostr). In the southern hemisphere, a similar anti-correlation is observed (Figures 5b and 5d). There, transport anomalies show comparable amplitudes as in the northern hemisphere and cross-correlation coefficients are lower for RG-clim

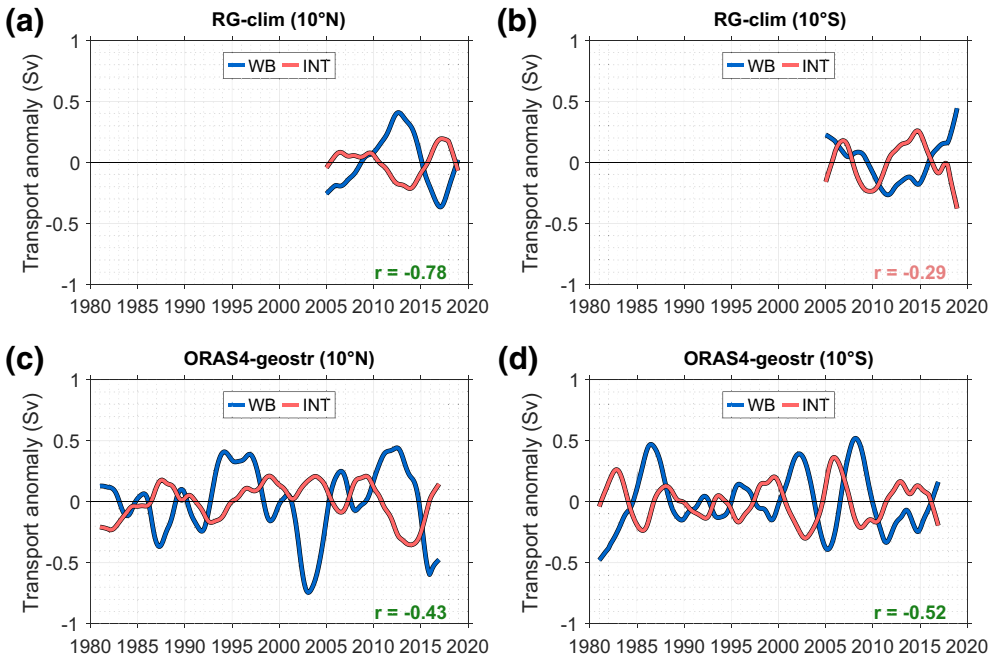

Figure 5. Time series of thermocline layer transport anomaly at 10°N (a and c) and 10°S (b and d) for RG-clim (a and b) and ORAS4-geostr (c and d). Transport anomalies are separated into a western boundary (WB; blue) and interior (INT; red) component within each hemisphere. A 2-year running mean is applied to all time series. Cross-correlation coefficients that are (not) significant at the 95% confidence interval are marked in green (red). Further details on the calculation of the cross-correlation coefficients and their significance are provided in the supporting information.

(−0.29) and about comparable for ORAS4-geostr (−0.52). Similar to 10°N, in the beginning of the time series, the anti-correlation in ORAS4-geostr is not as pronounced as it is in the later part from about 1996 onwards. Interestingly, although in the mean state of the Atlantic STCs, the northern hemisphere components only contribute about a third to the total mean convergence, their fluctuations show similar amplitudes compared to those in the southern hemisphere. In order to identify the dominant time scale of this anti-correlation a cross-spectral analysis was carried out (not shown) which does not favor a certain time scale but rather shows a similar anti-correlation at all-time scales. Longer time series will be needed to gain more insight into the time scale dependence of the WB versus INT relation.

Transport anomalies at the western boundary and in the interior are derived from integrated geostrophic velocities separated at a fixed longitude at 50°W (32°W) at 10°N (10°S) and are zonally cumulated. In order to find out which part of these zonal subsections dominates the WB and INT variability in each hemisphere we linearly regress the thermocline layer meridional geostrophic velocities at 25.5 kg m^{-3} point-by-point onto the interannual interior transport anomaly time series of both hemispheres (Figure 6).

Positive values indicate a strong connection between INT transport anomalies and geostrophic velocity anomalies on interannual time scales. In the northern hemisphere the zonal section along 10°N shows negative values at the western boundary and positive values east of 50°W confirming the previously described general anti-correlation between WB and INT. In the southern hemisphere, the INT transport anomalies are mainly driven by geostrophic velocity anomalies between 30° and 20°W which are clearly anti-correlated with geostrophic velocity anomalies at the western boundary. In the eastern part, seasonal outcropping at this particular isopycnal further emphasizes the role of the western part of the interior subsection for the overall INT transport anomalies on interannual time scales. The linear regression of geostrophic velocity anomalies onto the hemispheric WB transport anomaly (not shown) reveals a much wavier pattern suggesting a larger role of, for example, Rossby waves which are excited close to the western boundary due to wind stress changes.

From the mean state of the STCs, it is known that about three times more equatorward transport occurs at 10°S compared to 10°N. Is this interhemispheric asymmetry also observed for interannual fluctuations?

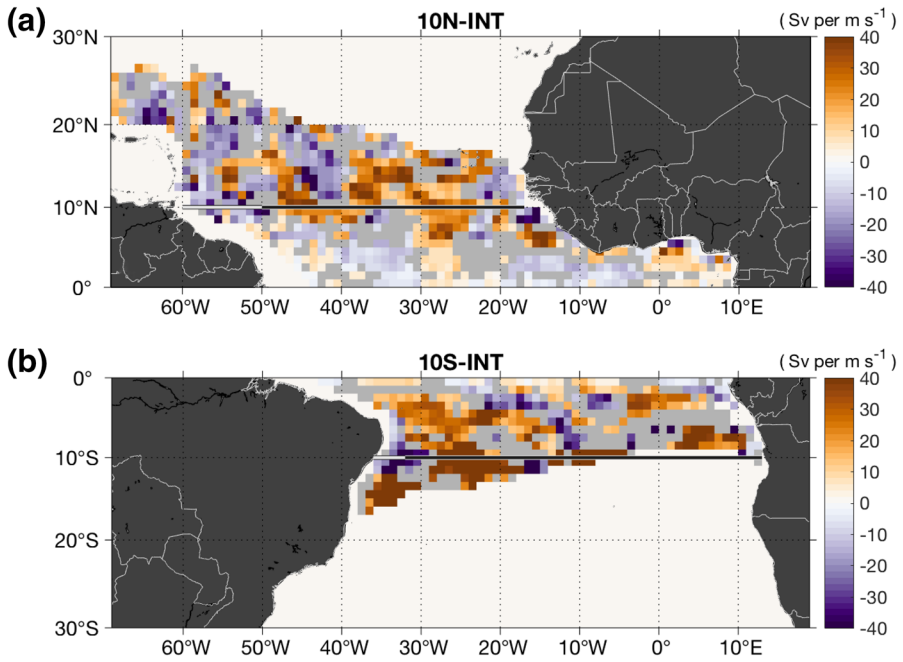

Figure 6. Linear regression of meridional geostrophic velocity anomalies (25.5 kg m^{-3} isopycnal) onto the interior thermocline layer transport anomaly for (a) the northern hemisphere and (b) the southern hemisphere from RG-clim. Statistically insignificant values are masked in gray. Shown are only grid points without seasonal outcropping of the 25.5 kg m^{-3} isopycnal. The zonal sections at 10°N and 10°S and their division into western boundary (white) and interior (black) are superimposed. A 2-year running mean is applied to the time series.

In order to find out which hemisphere ultimately dominates the interannual variability of the overall thermocline layer transport convergence, we use the combined hemispheric components (WB + INT) of the STCs. It shows that the thermocline layer transport convergence anomaly of the STCs undergoes an about pentadal oscillation (Figure 7).

RG-clim data reveal a weakening of thermocline layer transport convergence of about 1 Sv from the beginning of the time series in 2005–2010 (Figure 7a). From then on, the thermocline layer transport convergence strengthened by about 1 Sv over a time period of 6 years. However, it appears that generally one hemisphere dominates the total convergence. For RG-clim, first, mainly the southern hemisphere is responsible for the mentioned weakening of the thermocline layer transport convergence followed by a phase of equal contribution from both hemispheres before a strengthening of the northern hemisphere STC causes the total convergence to also strengthen.

This change of dominant hemisphere is also found for the thermocline layer transport convergence anomaly time series from ORAS4-geostr (Figure 7b). Besides agreeing on the dominant hemisphere for the time period in which both data products overlap, it further shows that before 2005 the northern hemisphere apparently dominated the thermocline layer transport convergence anomaly for about 15 years.

4.3. Impact on Sea Surface Temperature Variability

The STCs connect the subtropical subduction regions with tropical upwelling areas along the equator and at the eastern boundary. In this section, we analyze the connection of the different horizontal STC branches to equatorial SST variability on interannual to decadal time scales and discuss the observed time lags between the different STC components.

Smoothed time series (2-year running mean) of thermocline layer transport convergence anomalies from RG-clim and ORAS4-geostr are in good agreement and show variations on interannual to decadal time scales (Figure 8a). They lead equatorial SST anomalies by about 2–3 years (Figure 8b). The particular cross-correlation coefficients at zero lag are small (Figure 8a). Here, SST anomalies are based on a spatial

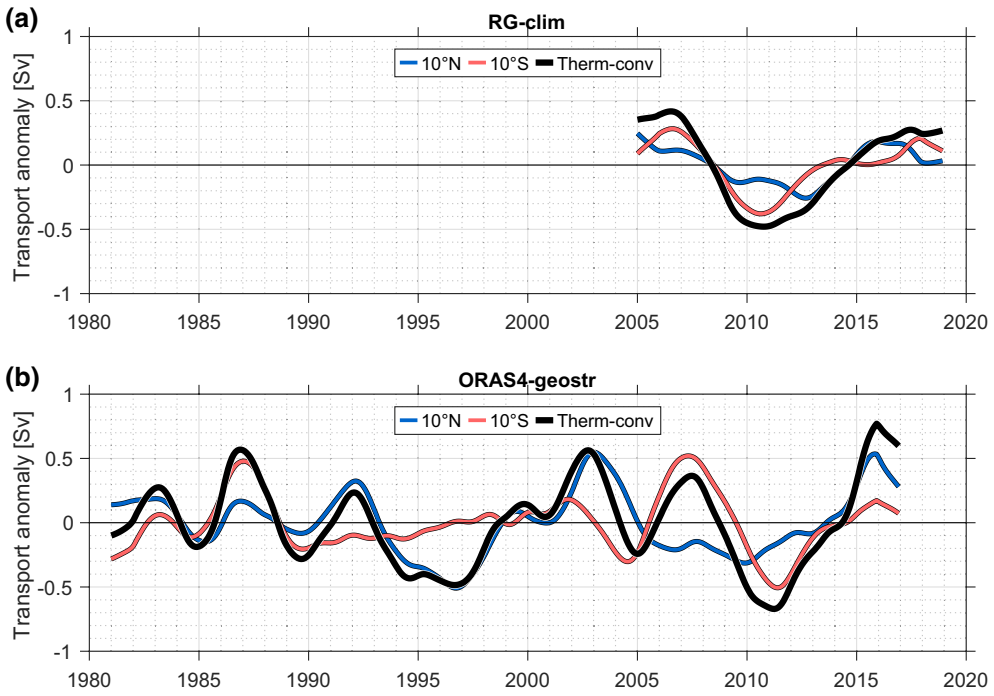

Figure 7. Time series of thermocline layer transport anomalies for (a) RG-clim and (b) ORAS4. Thermocline layer transport convergence anomalies (black) are separated into their northern hemisphere (blue) and southern hemisphere (red) component. A 2-year running mean is applied to the time series.

average between 30°W to 10°W and 3°S to 1°N, where we find the strongest relation in a lag regression analysis of SST anomalies onto interior transport convergence anomalies (described in more detail in the later part of this section). Transport anomalies vary between ±0.7 Sv while SST anomalies are mainly observed in a range between ±0.4°C. Notably, the cross-correlation indicates that stronger thermocline layer transport is followed by warmer SSTs.

For the Ekman divergence ($r = -0.50$) and the net surface layer transport divergence anomalies ($r = -0.48$), we find considerable anti-correlations at zero lag (Figure 8c). However, maximum cross-correlation occurs when the surface layer transport anomalies lead SST anomalies by about 3 months while Ekman transport anomalies lag SST anomalies by about 4 months (Figure 8d).

When considering variability on longer time scales (here accomplished by applying a 5-year running mean to all time series), the sign of the previously observed time lags is not affected but the lags are more pronounced (Figures 9b and 9d). At these time scales, thermocline layer transport convergence anomalies appear to be clearly leading SST anomalies (Figure 9a) but curiously, an increase of thermocline layer transport appears to be again related to increased equatorial SST. In the surface layer, the time lags increase for both ERA5 and ORAS4-total and the anti-correlations decrease at longer time scales but are still visible in the second half of the time series (Figures 9c and 9d) possibly indicating less time scale dependence in terms of connection to equatorial SST anomalies than in the thermocline layer.

Following the results from the previous Section 4.2, it is suggested that by analyzing the total thermocline layer transport convergence anomaly the individual contributions of the interior and western boundary components could be compensating each other. We therefore split the total thermocline layer transport convergence into a western boundary convergence and an interior convergence (Figure 10) with the same boundaries as defined in Section 3.1 (as indicated in Figure 1) and analyze the observed variability both on shorter (2-year running mean smoothing) and longer (5-year running mean smoothing) time scales. For RG-clim the zero lag cross-correlation with SST anomalies increases drastically when considering only the interior convergence ($r = -0.84$) while the convergence at the western boundary is positively correlated to SST anomalies ($r = 0.57$) for the 2-year running mean case (Figure 10a).

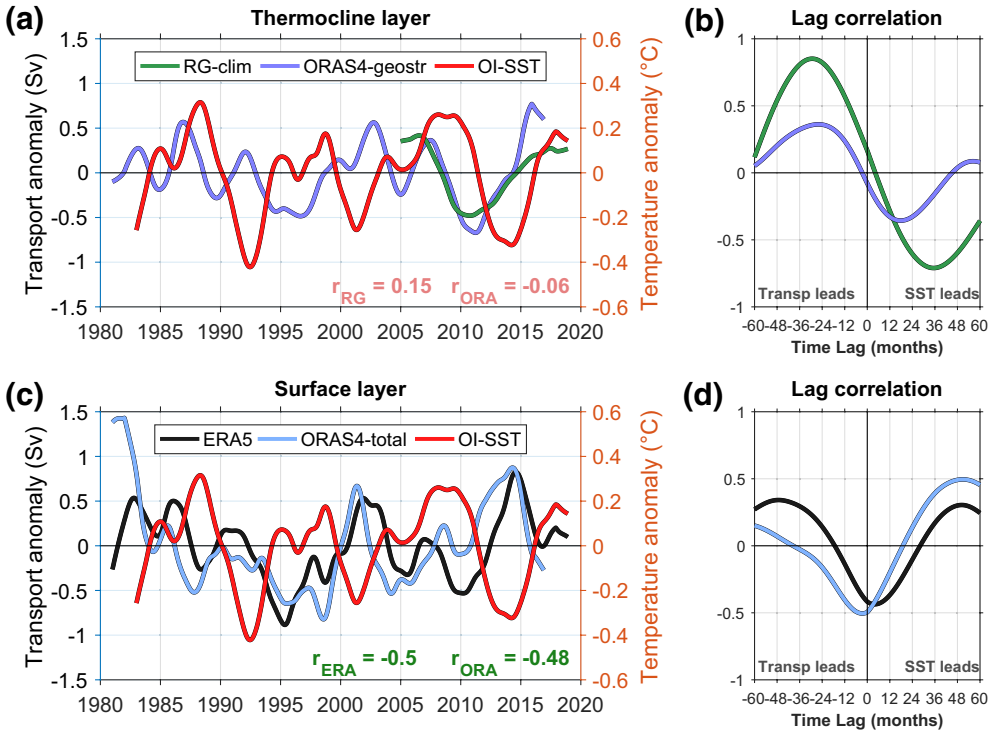

Figure 8. (a) Time series of anomalous thermocline layer transport convergence from RG-clim (green) and ORAS4-geostr (blue) with equatorial Atlantic (30°–10°W, 3°S–1°N) sea surface temperature (SST) anomaly from OI-SST (red) and (b) lag correlation analysis between the SST anomaly time series and RG-clim (green) and ORAS4-geostr (blue) thermocline layer transport convergence anomalies. (c) Time series of anomalous Ekman transport divergence from ERA5 (black), anomalous surface layer transport divergence from ORAS4 (light blue) and the same equatorial SST anomaly from OI-SST (red) as above and (d) lag correlation analysis between the SST anomaly time series and ERA5 (black) and ORAS4 (light blue) transport divergence anomalies. A 2-year running mean is applied to all time series. Cross-correlation coefficients that are (not) significant at the 95% confidence interval are marked in green (red). Further details on the calculation of the cross-correlation coefficients and their significance are provided in the supporting information.

However, RG-INT lags SST anomalies by 2 months while RG-WB is leading SST anomalies by about 1 year (Figure 10b). At first, the lag between RG-INT and SST might be counterintuitive. However, Klinger et al. (2002) and also Capotondi et al. (2005) noted for the Pacific Ocean that SST anomalies lead interior transport anomalies as well. Capotondi et al. (2005) attributed this striking temporal order to the continuous zonal evolution of the STCs at 10°N/10°S. They suggested that by zonally averaging along these sections an artificial time lag could evolve.

Another possible explanation could be that SST and interior transport convergence anomalies are fluctuating more or less in parallel and are not impacting each other at shorter time scales. Initially, changes in zonal wind stress force anomalous Ekman transport and a net surface divergence anomaly evolves which, on the one hand, drives equatorial SST anomalies with a small temporal lag. On the other hand, by changing equatorial upwelling rates, the EUC must respond to less (more) demand of water with a weakening (strengthening) transport which ultimately affects the interior STC branches as a supplier of the EUC (e.g., Rabe et al., 2008). By the time, this signal reaches the interior transport branches, equatorial SST has already reacted to the wind forcing and appears to lead the interior transport convergence. Therefore, at shorter time scales, the interior thermocline layer branches of the STCs are suggested to not have a direct impact on equatorial SST but could rather respond with some delay to the same surface wind forcing.

For anomaly time series smoothed with a 5-year running mean, we find a comparable anti-correlation between interior transport convergence anomalies and equatorial SST anomalies, but both RG-INT and ORA-INT now lead SST anomalies with a lag of about 2 months in RG-INT and a longer lag of about 6 months in ORA-INT (Figure 10d). Importantly, the correlation between interior transport convergence and SST

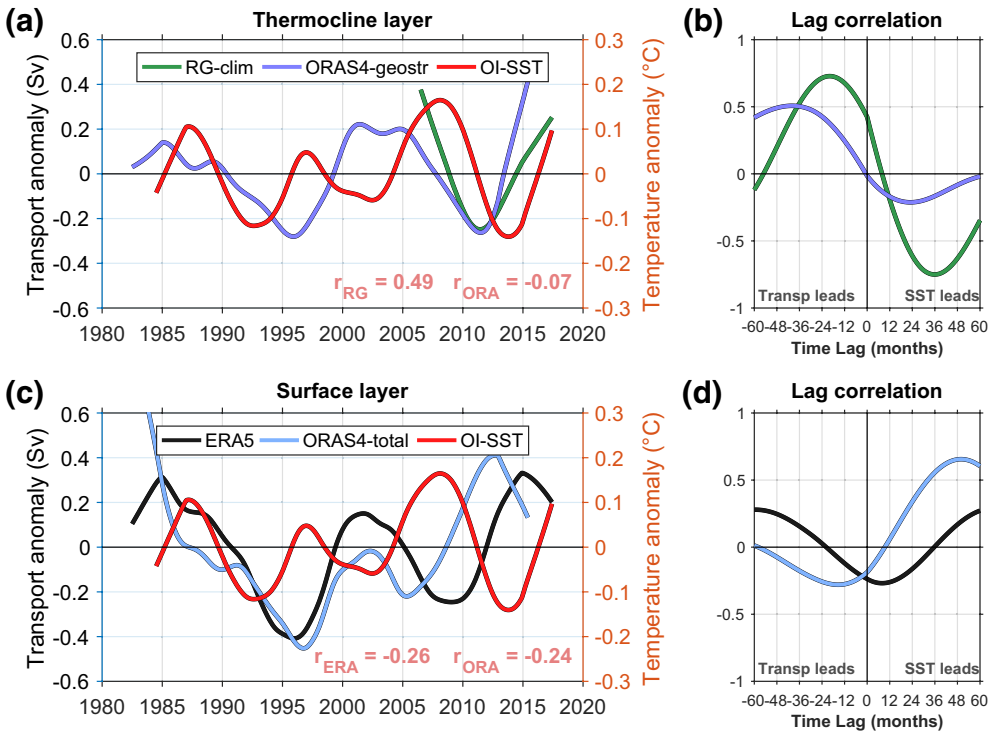

Figure 9. Same as Figure 8 but with a 5-year running mean applied to all time series.

anomalies is negative on these time scales, implying that stronger (weaker) interior transport is related to lower (higher) SSTs, in agreement with studies for the Pacific Ocean (e.g., McPhaden & Zhang, 2002, 2004).

The comparison between the results for the 2- and 5-year running mean time series suggests that the STCs are modulating equatorial SST rather on longer time scales which is consistent with model studies for the equatorial Pacific showing that while the SST variability on interannual time scales is predominantly driven by equatorial wind forcing, a significant part of the variability on decadal time scales is related to changes in the equatorward STC transport (Farneti et al., 2014; Lohmann & Latif, 2007; Lübbecke et al., 2008; Nonaka et al., 2002).

In order to quantify the SST response to STC changes, a linear point-by-point regression of the decadal (5-year running mean) RG-INT-CONV anomaly time series on decadal SST anomalies at the lag with maximum cross-correlation is carried out (Figure 11a). The SST response at this time lag reaches values of more than −2°C per Sv along an equatorial region between 30° and 10°W. Another region with a strong negative SST response to positive INT-conv changes exists in the eastern boundary upwelling region off Angola. In contrast to decadal variations in the lower STC branch, we have seen that changes in the upper horizontal branches of the STCs lead SST anomalies by about 12 months (Figure 9d). The SST response to surface layer transport anomalies shows the strongest regression coefficients in three regions: (1) southern central equatorial Atlantic, (2) along the eastern boundary upwelling off Mauritania and Senegal, and (3) along the Angolan upwelling region (Figure 11b).

Finally, the temporal and spatial role of wind for equatorial SST anomalies and the horizontal STC branches is examined both on interannual (2-year running mean) and on decadal time scales (5-year running mean). A lag correlation analysis between zonally averaged zonal wind stress anomalies at each latitude and equatorial SST anomalies (Figures 12a and 12b) reveals two findings. First, a relatively fast connection (correlation coefficients above 0.5) is observed between local zonal wind stress and equatorial SST anomalies at both time scales. This rather symmetric correlation about the zero lag is indicative of a positive feedback. Second, away from local forcing, the southern hemisphere appears to be more closely linked to equatorial SST anomalies as indicated by high correlation coefficients between 15° and 25°S with short time lag (Figure 12a). However, in the northern hemisphere, with a lag of about 2 years, we also find considerable correlation coefficients of more than 0.5 at both time scales.

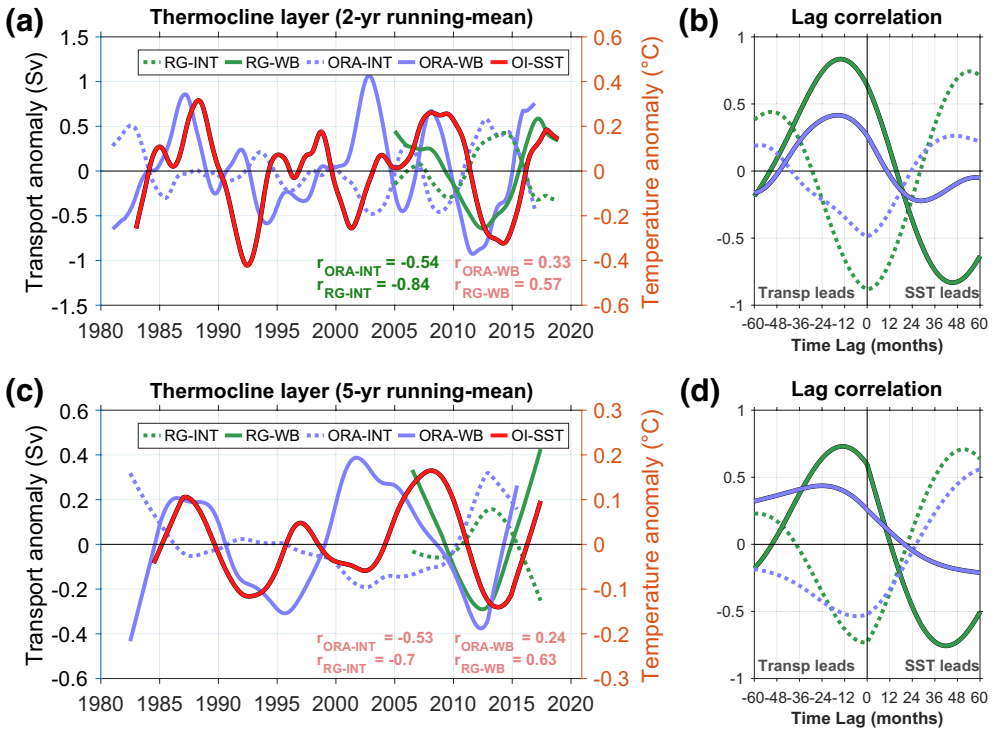

Figure 10. Time series of thermocline layer transport convergence anomaly divided into interior (dashed lines) and western boundary (solid lines) components for RG-clim (green) and ORAS4-geostr (blue) smoothed with (a) a 2-year running mean and (c) a 5-year running mean. Equatorial SST anomaly time series in (a) and (c) are the same as in Figures 8 and 9, respectively. The lag correlation analysis between the equatorial SST anomaly time series and individual thermocline layer transport convergence anomalies is shown for (b) 2-year running mean and (d) 5-year running mean smoothed time series. Cross-correlation coefficients that are (not) significant at the 95% confidence interval are marked in green (red). Further details on the calculation of the cross-correlation coefficients and their significance are provided in the supporting information.

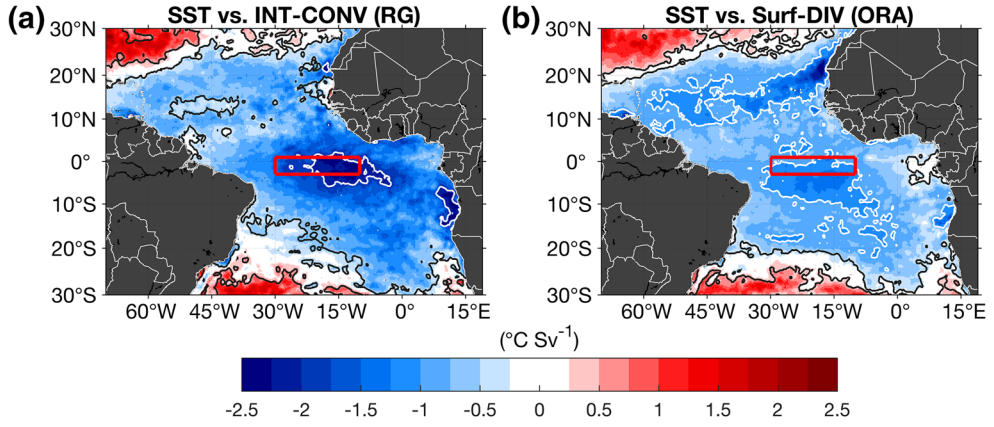

Figure 11. Linear regression of (a) interior transport convergence anomalies (RG-clim) and (b) surface transport divergence anomalies (ORAS4) point-by-point onto SST anomalies at the time lags defined in Figure 10a and Figure 9c: INT-CONV leads by 2 months and Surf-DIV leads by 12 months. The time lags are based on lag correlations between transport and equatorial SST anomalies (averaged within the red box). Black contours mark significant regression coefficients, whereas white contours mark regions where a transport anomaly of 1 Sv of INT-CONV (Surf-DIV) forces a negative SST anomaly of −2°C (−1°C). A 5-year running mean is applied to all time series.

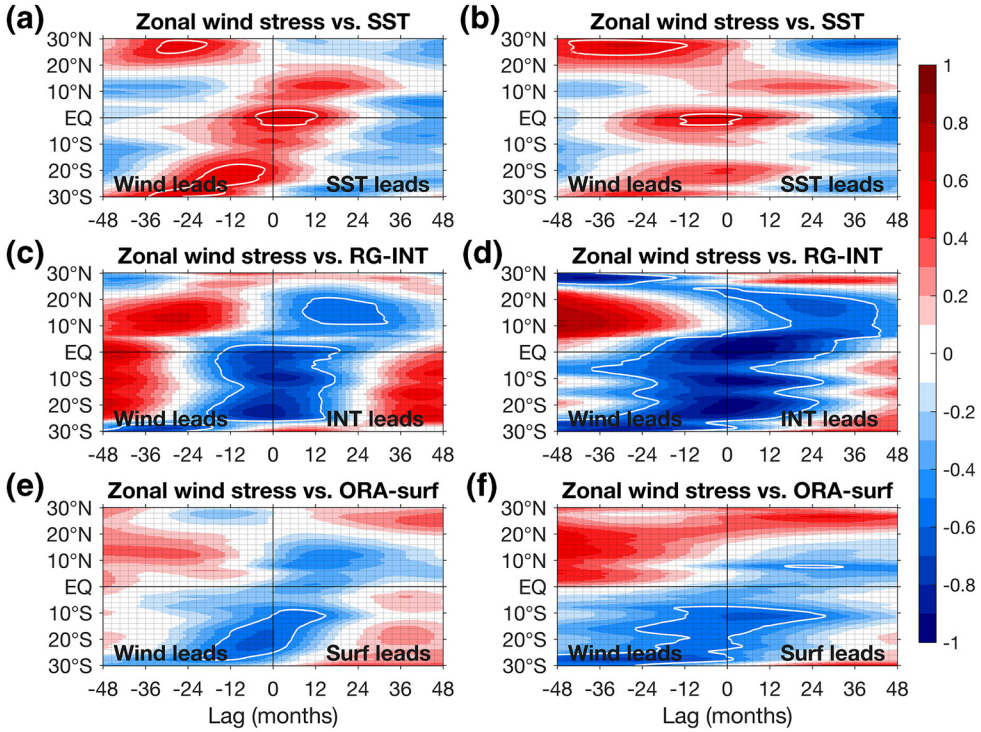

Figure 12. Lag correlation analysis as a function of latitude between ERA5 zonal wind stress anomalies and (a and b) equatorial SST anomalies (30°–10°W, 3°S–1°N), (c and d) interior transport convergence anomalies and (e and f) net surface layer transport divergence anomalies. All time series of the left (right) panels are smoothed by a 2-year (5-year) running mean. The −0.5 (0.5 for [a] and [b]) correlation isoline is marked by the white contours.

Previous model studies discussed the role of local versus remote forcing of equatorial SST variations, focusing on the Pacific. For instance, Nonaka et al. (2002) partly disagree with Kleeman et al. (1999) by showing that for decadal equatorial SST variations, the near-equatorial wind stress is as important as off-equatorial wind stress while Kleeman et al. (1999) proposed changes of wind stress and subduction mainly poleward of 23° to impact equatorial SST changes. However, the findings of Nonaka et al. (2002) have been questioned by Kröger et al. (2005) who showed that the relative contributions of equatorial and off-equatorial wind stress in driving SST variability on interannual to decadal time scales are significantly different. Most recently, Graffino et al. (2019) showed that equatorial SST anomalies are mainly driven by local wind stress anomalies while changes in the STC transport are rather forced by off-equatorial wind stress anomalies. For the interior STC convergence we observe maximum correlation with zonal wind stress anomalies south of the equator with the wind rather leading transport anomalies (Figure 12c). At longer time scales, the southern hemisphere still dominates interior transport anomalies (Figure 12d) and the highest correlations are observed at around 10°S and 20°S but also north of the equator.

Last, in the surface layer STC branch, off-equatorial zonal wind stress changes in the southern hemisphere dominate transport anomalies with close to no time lag around 10°S at both time scales (Figures 12e and 12f) indicating that mainly the south-easterly trade winds force the observed surface layer transport divergence between 10°N and 10°S.

5. Summary and Conclusion

In this study, the variability of transport associated with the individual horizontal branches of the Atlantic STCs and their impact on tropical SST variability on interannual to decadal time scales has been investigated by using a variety of observational and reanalysis products.

The study provides a first observational estimate of the temporal evolution of thermocline layer transport convergence and net surface layer transport divergence (Ekman + geostrophy). In both horizontal STC

branches, the seasonal cycle clearly dominates the time series (Figures 2 and 3). Thermocline layer transport convergence calculated between 10°N and 10°S shows a seasonal cycle with minimum values of about 7–9 Sv in boreal summer and maximum values of about 12–14 Sv in boreal winter. By separating the total thermocline layer transport convergence into its hemispheric and western boundary/interior components, we show that the western boundary in the northern hemisphere and the interior part of the southern hemisphere section dominate the observed annual cycle (Figures 2 and 4). While no statistically significant peaks are found on interannual or decadal time scales, which is likely a consequence of the rather short time period analyzed, the time series are clearly modulated on those longer time scales. Previous numerical studies also found rather small interannual variations of less than 2 Sv amplitude (Hüttl & Böning, 2006; Rabe et al., 2008). In the surface layer, the Ekman divergence between 10°N and 10°S exhibits a pronounced annual cycle of more than 10 Sv peak-to-peak amplitude (Figure 4) which is eventually reduced by an out-of-phase annual cycle of the surface geostrophic transport convergence. Comparison between different products for western boundary transports reveals considerable differences depending on data coverage and handling. Here, we made use of the 11°S mooring array providing almost 5 years of velocity data at the western boundary for the time period 2013–2018 (update of Hummels et al., 2015). We conclude that the seasonal cycle of western boundary transport is best captured by ORAS4 whereas the transport calculation from the Argo data product (RG-clim) underestimates the magnitude and shows larger differences in the seasonality of western boundary transport.

In a next step, we focused on the relation between interannual anomalies of western boundary and interior thermocline layer transports which are zonally separated at 50°W (32°W) in the northern (southern) hemisphere based on previous observational studies (Tuchen et al., 2019; Zhang et al., 2003). In both hemispheres, observations and reanalysis data show that contributions from the western boundary and the interior basin are anti-correlated and partially compensate each other (Figure 5). This relation is weakest for RG-clim in the southern hemisphere which is likely a consequence of the mentioned misrepresentation of magnitude and seasonality of western boundary current transport. However, to our knowledge, this relation has not yet been derived from observations but shown in numerical studies for the Pacific and Atlantic Ocean before. For the Pacific, Capotondi et al. (2005) show that variations at the western boundary and in the interior basin can both be associated with baroclinic Rossby wave adjustment. In their numerical study, large-scale changes of the wind stress curl drive instantaneous changes in the Ekman transport and Ekman pumping finally leading to changes of the subtropical gyres through an excitation of baroclinic Rossby waves. On their westward path, Rossby waves are suggested to first impact the interior parts of the basins before reaching the western boundary. Rossby waves alter the density structure and the zonal slope of the thermocline which eventually leads to changes in meridional transport. The higher the baroclinic mode and the further away from the equator the larger the lag between changes in the interior and changes at the western boundary. In this study, we find an almost instantaneous anti-correlation (Figure 5) suggesting that rather low-baroclinic-mode Rossby wave adjustment dominates. The highest anti-correlation is found at a time lag of about 1 month with the western boundary leading interior transport anomalies consistent with Rabe et al. (2008) but contradicting to the theory of westward propagating Rossby waves and emphasizing the possible role of locally generated Rossby waves. However, wind stress curl forcing in the western parts of the basins and poleward of 10°N/10°S could result in equatorward propagating coastally trapped waves whose signature is then observed in our western boundary transport components and could therefore distort the phase relation to interior transport anomalies.

Overall, the total thermocline layer transport convergence undergoes a weakening from 2005 to 2010 which is followed by a strengthening until about 2015/2016 (Figure 2). The northern hemisphere seems to dominate the recent strengthening while the southern hemisphere appears to be responsible for the previous weakening (Figure 7). However, reanalysis data suggest that previous interannual thermocline layer transport variations have been alternatingly dominated by contributions from the southern and northern hemisphere.

The final focus of this study was to analyze the impact of STC transport variability on equatorial SST variability at longer time scales. We observe the highest anti-correlations between anomalies of the interior part of the thermocline layer transport convergence and equatorial SST (−0.84 for RG-clim and −0.54 for ORAS4-geostr; Figure 10a). Including the western boundary thermocline layer transport convergence

drastically reduces this anti-correlation (Figures 8a and 9a) emphasizing the importance of the interior pathway as the link to the tropics. This is remarkable since, in the mean, the interior pathways are contributing less to the overall thermocline layer transport convergence but on pentadal time scales seem to be more closely related to SST variability. Another curious finding is that variations in the western boundary current transport and the total thermocline convergence are positively correlated with equatorial SST anomalies on both interannual and decadal time scales, suggesting that stronger STCs are associated with warmer SSTs. When considering thermocline layer convergence and surface layer divergence as the only contributors to the warm water volume (WWV) above the lower boundary of the thermocline layer (i.e., neglecting diapycnal transport), a thermocline layer convergence leads to an increase in WWV which is generally associated with an increase in SST. Our results suggest that on longer time scales thermocline layer convergence and the surface layer divergence anomalies are more correlated indicating a smaller impact on WWV changes so that rather an anti-correlation between thermocline layer convergence anomalies and SST anomalies is established. The relation of transport anomalies and WWV deserves further attention and will require further analysis.

In the Pacific, McPhaden and Zhang (2002, 2004) found an anti-correlation between interior meridional transport and tropically averaged SST, similar to our results for the interior convergence. However, in their studies, due to sparse observational data at the western boundary only the interior transport convergence could be related to SST variability and transport at the western boundary had to be derived as a residual between Ekman transport and interior transport. Also, the sparseness of observations forced the authors to calculate meridional transport in temporal bins of 7–10 years. Consequently, McPhaden and Zhang (2002) were not able to consider interannual variability and rather focused on decadal timescales. However, their analysis generally supports the $v'\overline{T}$ mechanism proposed by Kleeman et al. (1999). Our results partially question the previously assumed mechanism of how the thermocline layer branches of the STCs modulate equatorial SST temperature. It appears that only on longer time scales the STCs play a role in modulating SST anomalies along the equator and at the eastern boundary (Figures 10c and 11a). The coherence and phase spectrum between interior transport convergence and equatorial SST reassuringly shows a phase shift at a period of 5 years beyond which the interior transport convergence appears to lead equatorial SST anomalies (Figure S3). At shorter time scales the local wind stress forcing dominates SST changes (Figures 10a, 10b, 12a, and 12b). This is consistent with the findings of Rabe et al. (2008) who show that on time scales longer than 5 years to decadal an initial wind stress change is followed by, first, a response in the EUC and later in the STC transport convergence. However, in their study, the time lags between the responses of the different STC components were about 1 year which is considerably longer than observed in this analysis (Figure 10d).

The presented study aims to serve as a first observational estimate of transport variability associated with the Atlantic STCs. The absence of observational studies on Atlantic STC variability emphasizes the need for an analysis of the temporal evolution of the horizontal branches of the STCs and a discussion of their link to equatorial SST anomalies — a relation which for the Atlantic Ocean, so far, is only discussed in a few model studies. The presented results challenge the view of how the STCs have an impact on equatorial SST anomalies and provide approaches for future numerical models to further investigate this relation. However, the role of STC-driven SST anomalies in contrast or in combination with the tropical Atlantic modes remains unsolved and demands further analysis beyond the scope of this study. In addition, extensive observational efforts are needed to better resolve the spatial structure of the Atlantic STCs. Especially the western boundaries are sparsely sampled and introduce uncertainties to the analysis (Tuchen et al., 2019). Long-term mooring arrays and repeated ship sections in the tropical Atlantic (e.g., Hummels et al., 2015) are essential to resolve the temporal and spatial evolution of the Atlantic STCs.

Data Availability Statement

Horizontal displacement data from the updated YoMaHa*07 data set are available at http://apdrc.soest.hawaii.edu/projects/Argo/data/trjctry/. Reanalysis data from ORA-S4 can be accessed via ftp://ftp-icdc.cen.uni-hamburg.de/EASYInit/ORA-S4/monthly_1x1/. C-2015 ASCAT and QuikScat data are produced by Remote Sensing Systems and sponsored by the NASA Ocean Vector Winds Science Team. Data are available at www.remss.com. ERA5 monthly averaged data on single levels from 1979 to present is distributed by

the Copernicus Climate Change Service (C3S) (2017) under https://doi.org/10.24381/cds.f17050d7. ERA-interim monthly means of daily means can be accessed under https://apps.ecmwf.int/datasets/data/interim-full-moda/levtype=sfc/?month_years=1996&param=165.128,166.128. Microwave OI SST data are produced by Remote Sensing Systems and sponsored by National Oceanographic Partnership Program (NOPP) and the NASA Earth Science Physical Oceanography Program. Data are available at www.remss.com.

Acknowledgments
This study was supported by the German Federal Ministry of Education and Research (BMBF) as part of the BANINO project (03F0795A), RACE-Synthese (03F0824C) and by EU H2020 under grant agreement 817578 TRIATLAS project. We thank the captains, crews, scientists, and technicians involved in several research cruises with RV Meteor in the tropical Atlantic that contributed to collecting data used in this study. We further thank Rebecca Hummels for providing the interpolated moored velocity time series at the western boundary at 11°S. Open access funding enabled and organized by Projekt Deal. The authors would like to thank two anonymous reviewers for their helpful suggestions and comments.

References

Balmaseda, M. A., Mogensen, K., & Weaver, A. T. (2013). Evaluation of the ECMWF ocean reanalysis system ORAS4. *Quarterly Journal of the Royal Meteorological Society*, *139*, 1132–1161. https://doi.org/10.1002/qj.2063

Belmonte Rivas, M., & Stoffelen, A. (2019). Characterizing ERA-Interim and ERA5 surface wind biases using ASCAT. *Ocean Science*, *15*, 831–852. https://doi.org/10.5194/os-15-831-2019

Capotondi, A., Alexander, M. A., Deser, C., & McPhaden, M. J. (2005). Anatomy and decadal evolution of the Pacific Subtropical-Tropical cells (STCs). *Journal of Climate*, *18*(9), 3739–3758. https://doi.org/10.1175/JCLI3496.1

Carton, J. A., Cao, X., Giese, B. S., & Da Silva, A. M. (1996). Decadal and interannual SST variability in the tropical Atlantic Ocean. *Journal of Physical Oceanography*, *26*(7), 1165–1175. https://doi.org/10.1175/1520-0485(1996)026<1165:DAISVI>2.0.CO;2

Chang, P., Link, J., Li, H., Pendland, C., & Matrosova, L. (1998). Prediction of tropical Atlantic sea surface temperature. *Geophysical Research Letters*, *25*(8), 1193–1196. https://doi.org/10.1029/98GL00852

Dee, D. P., Uppala, S. M., Simmons, A. J., Berrisford, P., Poli, P., Kobayashi, S., et al. (2011). The ERA-interim reanalysis: Configuration and performance of the data assimilation system. *Quarterly Journal of the Royal Meteorological Society*, *137*(656), 553–597. https://doi.org/10.1002/qj.828

Farneti, R., Dwivedi, S., Kucharski, F., Molteni, F., & Griffies, S. M. (2014). On Pacific subtropical cell variability over the second half of the twentieth century. *Journal of Climate*, *27*(18), 7102–7112. https://doi.org/10.1175/JCLI-D-13-00707.1

Fratantoni, D. M., Johns, W. E., Townsend, T. L., & Hurlburt, H. E. (2000). Low-latitude circulation and mass transport pathways in a model of the tropical Atlantic Ocean. *Journal of Physical Oceanography*, *30*(8), 1944–1966. https://doi.org/10.1175/1520-0485(2000)030<1944:LLCAMT>2.0.CO;2

Graffino, G., Farneti, R., Kucharski, F., & Molteni, F. (2019). The effect of wind stress Anomalies and location in driving Pacific Subtropical cells and tropical climate. *Journal of Climate*, *32*(5), 1641–1660. https://doi.org/10.1175/JCLI-D-18-0071.1

Gu, D., & Philander, S. G. H. (1997). Interdecadal climate fluctuations that depend on exchanges between the tropics and extratropics. *Science*, *275*(5301), 805–807. https://doi.org/10.1126/science.275.5301.805

Hazeleger, W., de Vries, P., & Friocourt, Y. (2003). Sources of the Equatorial Undercurrent in a high-resolution ocean model. *Journal of Physical Oceanography*, *33*(4), 677–693. https://doi.org/10.1175/1520-0485(2003)33<677:SOTEUI>2.0.CO;2

Hazeleger, W., & Drijfhout, S. (2006). Subtropical cells and meridional overturning circulation pathways in the tropical Atlantic. *Journal of Geophysical Research*, *111*, C03013. https://doi.org/10.1029/2005JC002942

Hazeleger, W., Visbeck, M., Cane, M., Karspeck, A., & Naik, N. (2001). Decadal upper ocean temperature variability in the tropical Pacific. *Journal of Geophysical Research*, *106*, 8971–8988. https://doi.org/10.1029/2000jc000536

Hersbach, H., & Dee, D. (2016). ERA5 reanalysis is in production. *ECMWF Newsletter*, *147*, 7. https://www.ecmwf.int/en/newsletter/147/news/era5-reanalysis-production

Hummels, R., Brandt, P., Dengler, M., Fischer, J., Araujo, M., Veleda, D., et al. (2015). Interannual to decadal changes in the Western Boundary Circulation in the Atlantic at 11°S. *Geophysical Research Letters*, *42*, 7615–7622. https://doi.org/10.1002/2015GL065254

Hüttl, S., & Böning, C. W. (2006). Mechanisms of decadal variability in the shallow subtropical-tropical circulation of the Atlantic Ocean: A model study. *Journal of Geophysical Research*, *111*, C07011. https://doi.org/10.1029/2005JC003414

Kleeman, R., McCreary, J. P., & Klinger, B. A. (1999). A mechanism for generating ENSO decadal variability. *Geophysical Research Letters*, *26*(12), 1743. https://doi.org/10.1029/1999GL900352

Klinger, B., McCreary, J. P., & Kleeman, R. (2002). The relationship between oscillating subtropical wind stress and equatorial temperature. *Journal of Physical Oceanography*, *32*(5), 1507–1521. https://doi.org/10.1175/1520-0485(2002)032<1507:TRBOSW>2.0.CO;2

Kröger, J., Busalacchi, A. J., Ballabrera-Poy, J., & Malanotte-Rizzoli, P. (2005). Decadal variability of shallow cells and equatorial sea surface temperature in a numerical model of the Atlantic. *Journal of Geophysical Research*, *110*, C12003. https://doi.org/10.1029/2004JC002703

Lebedev, K. V., Yoshinari, H., Maximenko, N. A., & Hacker, P. W. (2007). YoMaHa'07: Velocity data assessed from trajectories of Argo floats at parking level and at the sea surface. *IPRC Technical Note*, *2*(4), 20.

Lee, T., & Fukumori, I. (2003). Interannual-to-decadal variations of the tropical-subtropical exchange in the Pacific Ocean: Boundary versus interior pycnocline transports. *Journal of Climate*, *16*, 4022–4042. https://doi.org/10.1175/1520-0442(2003)016<4022:IVOTEI>2.0.CO;2

Liu, Z., Philander, S. G. H., & Pacanowski, R. C. (1994). A GCM study of tropical-subtropical upper-ocean water exchange. *Journal of Physical Oceanography*, *24*(12), 2606–2623. https://doi.org/10.1175/1520-0485(1994)024<2606:AGSOTU>2.0.CO;2

Lohmann, K., & Latif, M. (2007). Influence of El Niño on the upper-ocean circulation in the tropical Atlantic Ocean. *Journal of Climate*, *20*, 5012–5018. https://doi.org/10.1175/JCLI4292.1

Lübbecke, J. F., Böning, C. W., & Biastoch, A. (2008). Variability in the subtropical-tropical cells and its effect on near-surface temperature of the equatorial Pacific: A model study. *Ocean Science*, *4*, 73–88. https://doi.org/10.5194/os-4-73-2008

Luo, Y., Rothstein, L. M., & Zhang, R.-H. (2009). Response of Pacific subtropical-tropical thermocline water pathways and transports to global warming. *Geophysical Research Letters*, *36*, L04601. https://doi.org/10.1029/2008GL036705

Luyten, J. R., Pedlosky, J., & Stommel, H. (1983). The ventilated thermocline. *Journal of Physical Oceanography*, *13*, 292–309. https://doi.org/10.1175/1520-0485(1983)013<0292:TVT>2.0.CO;2

Malanotte-Rizzoli, P., Hedstrom, K., Arango, H., & Haidvogel, D. B. (2000). Water mass pathways between the subtropical and tropical ocean in a climatological simulation of the North Atlantic Ocean circulation. *Dynamics of Atmospheres and Oceans*, *32*(3–4), 331–371. https://doi.org/10.1016/S0377-0265(00)00051-8

McCreary, J. P., & Lu, P. (1994). Interaction between the subtropical and equatorial ocean circulations: The subtropical cells. *Journal of Physical Oceanography*, *24*(2), 466–497. https://doi.org/10.1175/1520-0485(1994)024<0466:IBTSAE>2.0.CO;2

McPhaden, M. J., & Zhang, D. (2002). Slowdown of the meridional overturning circulation in the upper Pacific Ocean. *Nature*, *415*, 603–608. https://doi.org/10.1038/415603a

McPhaden, M. J., & Zhang, D. (2004). Pacific Ocean circulation rebounds. *Geophysical Research Letters*, *31*, L18301. https://doi.org/10.1029/2004GL020727

Nonaka, M., Xie, S.-P., & McCreary, J. P. (2002). Decadal variations in the subtropical cells and equatorial Pacific SST. *Geophysical Research Letters*, *29*, 1116. https://doi.org/10.1029/2001GL013717

Oschlies, A., Brandt, P., Stramma, L., & Schmidtko, S. (2018). Drivers and mechanisms of ocean deoxygenation. *Nature Geoscience*, *11*(7), 467–473. https://doi.org/10.1038/s41561-018-0152-2

Rabe, B., Schott, F. A., & Köhl, A. (2008). Mean circulation and variability of the tropical Atlantic during 1952-2001 in the GECCO assimilation fields. *Journal of Physical Oceanography*, *38*(1), 177–192. https://doi.org/10.1175/2007JPO3541.1

Reynolds, R. W., Smith, T. M., Liu, C., Chelton, D. B., Casey, K. S., & Schlax, M. G. (2007). Daily high-resolution-blended Analyses for sea surface temperature. *Journal of Climate*, *20*, 5473–5496. https://doi.org/10.1175/2007JCLI1824.1

Ricciardulli, L., & Wentz, F. J. (2016). *Remote sensing systems ASCAT C-2015 daily ocean vector winds on 0.25 deg grid, version 02.1*. Santa Rosa, CA: Remote Sensing Systems. Available online at www.remss.com/missions/ascat

Ricciardulli, L., Wentz, F. J., & Smith, D. K. (2011). *Remote sensing Systems QuikSCAT Ku-2011 Ocean Vector winds on 0.25 deg grid, version 4*. Santa Rosa, CA: Remote Sensing Systems. Available online at www.remss.com/missions/qscat

Roemmich, D., & Gilson, J. (2009). The 2004-2008 mean and annual cycle of temperature, salinity, and steric height in the global ocean from the Argo Program. *Progress in Oceanography*, *82*(2), 81–100. https://doi.org/10.1016/j.pocean.2009.03.004

Schott, F. A., Brandt, P., Hamann, M., Fischer, J., & Stramma, L. (2002). On the boundary flow off Brazil at 5-10°S and its connection to the interior tropical Atlantic. *Geophysical Research Letters*, *29*(17), 1840. https://doi.org/10.1029/2002GL014786

Schott, F. A., Dengler, M., Zantopp, R., Stramma, L., Fischer, J., & Brandt, P. (2005). The shallow and deep western boundary circulation of the South Atlantic at 5°–11°S. *Journal of Physical Oceanography*, *35*(11), 2031–2053. https://doi.org/10.1175/JPO2813.1

Schott, F. A., McCreary, J. P., & Johnson, G. C. (2004). Shallow overturning circulations of the tropical-subtropical oceans. *Earth Climate: The Ocean-Atmosphere Interaction. Geophysical Monography Series*, *147*, 261–304. https://doi.org/10.1029/147GM15

Schott, F. A., Wang, W., & Stammer, D. (2007). Variability of Pacific subtropical cells in the 50-year ECCO assimilation. *Geophysical Research Letters*, *34*, L05604. https://doi.org/10.1029/2006GL028478

Stramma, L., Fischer, J., & Reppin, J. (1995). The North Brazil Undercurrent. *Deep-Sea Research I*, *42*, 773–795. https://doi.org/10.1016/0967-0637(95)00014-W

Tuchen, F. P., Lübbecke, J. F., Schmidtko, S., Hummels, R., & Böning, C. W. (2019). The Atlantic subtropical cells inferred from observations. *Journal of Geophysical Research: Oceans*, *124*, 7591–7605. https://doi.org/10.1029/2019JC015396

Zhang, D., & McPhaden, M. J. (2006). Decadal variability of the shallow Pacific meridional overturning circulation: Relation to tropical sea surface temperatures in observations and climate change models. *Ocean Modeling*, *15*, 250–273. https://doi.org/10.1016/j.ocemod.2005.12.005

Zhang, D., McPhaden, M. J., & Johns, W. E. (2003). Observational evidence for flow between the subtropical and tropical Atlantic: The Atlantic subtropical cells. *Journal of Physical Oceanography*, *33*, 1783–1797. https://doi.org/10.1175/2408.1